DOI: 10.1002/((please add manuscript number))

Article type: Communication

Enhancing Doping Efficiency by Improving Host-Dopant Miscibility for Fullerene-Based n-Type Thermoelectrics[†]

Li Qiu,[‡a,b] *Jian Liu,*[‡a] *Riccardo Alessandri,*[a,c] *Xinkai Qiu,*[a,b] *Marten Koopmans,*[a] *Remco W. A. Havenith,*[a,b,d] *Siewert J. Marrink,* [a,c] *Ryan C. Chiechi,*[a,b] *L. Jan Anton Koster* [*a] *and Jan C. Hummelen* [*a,b]

[a] *Zernike Institute for Advanced Materials, University of Groningen, Nijenborgh 4, 9747 AG Groningen, The Netherlands*

[b] *Stratingh Institute for Chemistry, University of Groningen, Nijenborgh 4, 9747 AG Groningen, The Netherlands*

[c] *Groningen Biomolecular Sciences and Biotechnology Institute, University of Groningen, Nijenborgh 7, 9747 AG Groningen, The Netherlands*

[d] *Ghent Quantum Chemistry Group, Department of Inorganic and Physical Chemistry, Ghent University, Krijgslaan 281 (S3), B-9000 Gent, Belgium*

E-mail: l.j.a.koster@rug.nl; j.c.hummelen@rug.nl

[†] Electronic Supplementary Information (ESI) available: [details of any supplementary information available should be included here]. See DOI: 10.1039/b000000x/

[‡] These two authors contributed equally to this work.

Keywords: Organic Thermoelectrics, Seebeck Coefficient, n-Doping, Miscibility, Fullerene derivatives

Abstract

This paper describes a promising n-type doping system with high performance for thermoelectric applications. By introducing polar triethylene glycol (TEG) side chain onto both fullerene host (PTEG-1) and dopant (TEG-DMBI) materials, the TEG-DMBI doped PTEG-1 films obtained through solution processing provide a better miscibility compared with films doped with commercially available N-DMBI (bearing a dimethylamino group instead of TEG), as determined by phase imaging AFM (atomic force microscopy) measurements and coarse-grain molecular dynamics simulations, leading to high doping efficiency of up to 18% at 20 mol% doping concentration and thus high carrier density and mobility, which are critical to the electrical conductivity. Therefore a record power factor of 19.1 $\mu Wm^{-1}K^{-2}$ is obtained with an electrical conductivity of 1.81 Scm^{-1} , one of the highest values reported for solution processable fullerene derivatives as n-type organic materials for thermoelectric applications to date.

1. Introduction

Organic semiconductors (OSCs) have attracted extensive interest in terms of their potential for thermoelectric applications [1–7] due to both mechanical flexibility and solution processability, enabling lightweight, low cost, and flexible electricity generation modules. [8–10] The thermoelectric energy conversion (from heat to electricity) efficiency is defined by the thermoelectric figure-of-merit $ZT=S^2\sigma T/\kappa$, where S is the Seebeck coefficient, σ is the electrical conductivity, T is the absolute temperature and κ is the thermal conductivity. For OSCs, κ is intrinsically low (much lower than traditional inorganic semiconductors and typically has a value below 1 $Wm^{-1}K^{-1}$), [11–16] making them promising for use in thermoelectric applications. Meanwhile, the variation in κ is relatively small and secondary to modulation in σ and S, thermoelectric property of a material can therefore be weighted with thermoelectric power factor ($S^2\sigma$) in $Wm^{-1}K^{-2}$: the larger the power factor, the better performance of the material. For the optimization of power factor, doping is regarded as the key strategy, [17–29] because it determines free-carrier concentration (and hence S) and affects carrier mobility. More specifically, due to the weak van der Waals bonding characteristic of OSCs, the effect of dopants on carrier transport properties is especially large (in comparison to their inorganic counterparts). [26] Therefore, the doping could be expected to be an effective way to enhance the performance of OSCs in the thermoelectric applications, which traditionally suffer from low power factor.

Compared with the progress made on p-doping, n-doping is lagging behind due to the difficulty in finding efficient dopants for n-type semiconductors, which could partially account for the current situation that, unlike their p-type counterparts, [22–32] the development of n-type organic thermoelectric materials have not progressed rapidly, [33–36] but which is required for practical thermoelectric device applications. Most of the reported n-dopants thus far, such as reactive alkali

metals, cationic dyes, or organometallic complexes, either possess poor ambient stability or require strict vacuum processing. Recently, an efficient solution-processable n-type dopant, N-DMBI, namely (4-(1,3-dimethyl-2,3-dihydro-1H-benzoimidazol-2-yl)phenyl)dimethylamine was developed by Bao and co-workers and a σ of 1.9×10^{-3} Scm^{-1} was therefore achieved by doping solution-processed PCBM (Phenyl-C61-butyric acid methyl ester) films (vs 8.1×10^{-8} Scm^{-1} for undoped PCBM film).[37] Since then, N-DMBI and its analogues have attracted extensive attention in development of solution processed n-type OSCs, including but not limited to thermoelectric materials, e.g., Bao et al. then demonstrated the use of 1H-benzoimidazole derivatives to dope graphene efficiently by solution processing such as spin-coating and inkjet printing [38] and to tune the charge carrier density of carbon nanotubes films to control the threshold voltages of carbon nanotube transistors precisely.[39] Meanwhile, Bao et al. also reported that neutral dimeric dopants $(DMBI)_2$ could exhibit a stronger doping effect compared with previously reported DMBI dopants in a more diverse array of materials, ranging from polymers to fullerene derivatives.[40,41] Later, Chabinyc and co-workers reported that solution mixtures of P(NDIOD-T2)(poly[N,N'-bis(2-octyldodecyl)-naphthalene-1,4,5,8-bis(dicarboximide)-2,6-diyl]-alt-5,5'-(2,2'-bithiophene)) with N-DMBI and its analogue achieved electrical conductivities of nearly 10^{-2} Scm^{-1} and power factors of up to 0.6 $\mu Wm^{-1}K^{-2}$.[27] More recently, Pei and co-workers demonstrated that three n-type benzodifurandione-based PPV polymers exhibit outstanding electrical conductivities of up to 14 Scm^{-1} and power factors up to 28 $\mu Wm^{-1}K^{-2}$ when mixed with N-DMBI in solution, achieving the highest reported value for solution processable n-type polymers to date.[42]

As one of the best n-type semiconductors [43], fullerenes have been widely used in the last decade in organic solar cells (OSCs) [44,45], organic transistors [46] and molecular wires [47], but their thermoelectric properties have not yet been well studied. Due to their high intrinsic electron

mobility, high σ can be expected when a moderate number of charge carriers is provided by interfacial doping. Early studies focused on the n-doped [60]fullerene (C_{60}) conducting films through vacuum deposition of several types of n-dopants including alkaline metals, metal complexes and salts. [48–53] The highest power factor for the Cs_2CO_3/C_{60} bilayer structure and single layer blend device was found to be 20.5 and 28.8 $\mu Wm^{-1}K^{-2}$ respectively, [51,53] which are roughly comparable to the best performing n-type organometallic polymer thermoelectric material up to date with a power factor of up to 66 $\mu Wm^{-1}K^{-2}$. [33] However, these methods (dopants) are not amenable to solution-processing, severely restricting their extensive applications. Recently, we demonstrated that, by tailoring host-dopant miscibility, N-DMBI doped PTEG-1 (structures shown in Fig. 1) film exhibited the best result for solution-processed doped fullerene derivative films with σ of 2.05 Scm^{-1} and power factor of 16.7 $\mu Wm^{-1}K^{-2}$, [54] the electric conductivity is much higher than most of the previously reported values for the solution processable n-type materials: more than 3 or 2 orders of magnitude higher than N-DMBI doped PCBM [37] and naphthalene-based polymer [27] respectively, even if still lower than the record value (14 $Scm^{-1)}$ of doped benzodifurandione-based PPV polymers, [42] while the obtained power factor could even rank amongst the highest values for solution processable n-type materials.

Encouraged by the above promising results, we designed and synthesized a new DMBI dopant incorporating same polar triethylene glycol (TEG) side chain, namely TEG-DMBI, targeting better dopant/host miscibility (vs PTEG-1/N-DMBI system) by taking advantage of oligo (ethylene glycol) intermolecular interactions. Although no obvious aggregates on the surfaces were observed with AFM for both doped systems, phase imaging AFM studies and coarse-grain molecular dynamics simulations indicate that the morphology of this system is better than that of PTEG-1/N-DMBI system, implying improved host/dopant miscibility. This finding indicates the host/dopant

miscibility can be tailored by the control of the structural similarity between two components, opening a gate for future molecular design for n-type dopants. The PTEG-1/TEG-DMBI system exhibits the highest electric conductivity of 1.93 Scm^{-1} and power factor of 19.1 $\mu Wm^{-1}K^{-2}$ at doping concentration of 20 mol%, representing the best result in thermoelectric application for solution-processed n-type fullerene derivatives .

2. Results and Discussion

To characterize the thermoelectric properties of doped PTEG-1 films, the electrical conductivity and Seebeck coefficient were examined. Thin films were prepared from solution mixtures of PTEG-1 and TEG-DMBI in varied molar fractions by spin-coating on glass substrates, followed by deposition of Au electrodes as the top contacts with channel lengths of 100-300 μm, which were then subjected to thermal annealing at 120 °C for 1.5 h. The control devices based on the N-DMBI-doped PTEG-1 films were fabricated as well, following the same procedure. Electrical conductivity was measured via a two-probe method, and the Seebeck coefficient was determined by imposing a temperature difference across the sample and measuring the thermovoltage. As shown in Fig. 2, the electrical conductivities and thus power factors of the films dramatically increase by adding the dopant, and attain maxima as the molar fraction of dopant in solution is 20% for TEG-DMBI and 40% for N-DNBI respectively. The negative Seebeck coefficients demonstrate that n-type electrical transport is dominant, persisting with the n-type character of fullerenes. When the electrical conductivities increase, the Seebeck coefficients change in opposite direction, which is consistent with their opposite dependences on free-carrier concentrations. Further increasing the concentration of dopant leads to a rapid decrease of electrical conductivities and the Seebeck coefficients keep declining, possibly due to the disturbing effect of overloaded dopant.[26] Comparing Fig. 2A and 2B, the introduction of TEG chain (on TEG-DMBI) instead of dimethylamino group (on N-DMBI) of

the dopant has a remarkable influence on the evolution of σ, S and power factor in doping concentrations. While the optimal σ of 1.93 Scm^{-1} (with S of -291 μV/k) and power factor of 16.3 $\mu Wm^{-1}K^{-2}$ for N-DMBI doped PTEG-1 films are obtained at 40 mol% doping concentration which are almost identical with those we reported before, [54] comparable σ of 1.81 Scm^{-1} (with S of -325 μV/k) and (≈ 20%) higher power factor of 19.1 $\mu Wm^{-1}K^{-2}$ for TEG-DMBI doped PTEG-1 films are achieved at only 20 mol% doing concentration, which is the best thermoelectric performance for solution processable C_{60} derivatives with one of the highest σ and the record power factors to date. These results indicate modification of the structure of the dopant not only affects the thermoelectric performance including σ and power factor of the doped fullerene system, but also the doping efficiency (see below for discussions).

Because power factor and σ are sensitive to the carrier concentration, we then interpreted, like we did for the N-DMBI doped PTEG-1 system,[54] the charge transport behavior in the doped C_{60} derivative system can be described by using extended Gaussian disorder model (EGDM).[63] According to EGDM, the charge carriers in disordered organic semiconductors hop over an energy landscape with a Gaussian density of states (DOS), which is considered a thermally activated process. The charge hopping mobility largely depends on the temperature and on the carrier density. In our previous study on doped fullerene derivatives,[61] we managed to develop a relationship between the activation energy and charge carrier density for varying disorder parameters based on EGDM. (The details of this method is reported in that paper and also shown in Supporting Information.) Previously we got the activation energies from Arhenius fitting of variable temperature conductivities. It was found for doped PTEG-1 system these obtained activation energies were consistent perfectly with those obtained directly from Seebeck coefficient values by using the following formula: [52]

$$E_S = |S| \cdot T \cdot e \qquad (1)$$

Where E_S, T and e were activation energy, absolute temperature and elementary charge, respectively. Therefore, based on our measured Seebeck coefficient values in Fig. 2, the activation energies of differently doped PTEG-1 thin films were derived using formula 1 and displayed in Fig. 3A. The doped PTEG-1 thin films by both dopants showed the same trend of E_S decreasing with increasing doping concentration, indicating that the Fermi level shifts towards the LUMO. However, The TEG-DMBI doped PTEG-1 films showed more rapid decrease from 154 to 98 meV in activation energies from 10 mol% to 20 mol% doping concentration when compared with N-DMBI doped PTEG-1 films (from 156 to 114 meV). The smaller activation energy for TEG-DMBI doped PTEG-1 films indicates larger population of charge carriers filling the tail of density of states (DOS). By simply adapting our activation energies into our developed relationship between activation energy and charge carrier density, the carrier densities in different doping systems was obtained (Fig. 3B). It should be pointed out we assume that the charge carrier density generated by molecular doping is independent on the temperature in the vicinity of room temperature. As observed in doped PTEG-1 systems, carrier density keeps increasing with the doping concentration. While the plot for N-DMBI is linear, TEG-DMBI experiences, an exponential increase and then grows steadily larger. At minor or moderate doping level (i.e., 20 mol%) TEG-DMBI exhibits better doping efficiency. The peak doping efficiency of 10% and 18% for N-DMBI and TEG-DMBI respectively was obtained at doping concentration of 20 mol%, which means 10% of introduced N-DMBI vs 18% of TEG-DMBI molecules are active and donate electrons to host molecules in PTEG-1 matrix. The charge carrier densities of 3.6×10^{19} cm^{-3} for TEG-DMBI and 2.0×10^{19} cm^{-3} for N-DMBI were achieved in the doped PTEG-1 films with 20% dopant according the reported N = 10^{21} cm^{-3} for C_{60} based materials. [56] The high charge carrier densities indicate in turn PTEG-1 was heavily doped in both systems. The mobility values thus obtained based on the formula ($\mu = \sigma /$

$n \cdot e$) from charge carrier densities (Fig. S2 in Supporting Information) of different doped films afford a positive dependence, like carrier density, on the doping levels before reaching the maxim σ, which means the fast increase in σ with the doping level comes from both of the increased carrier density and mobility, and the much faster one for TEG-DMBI confirms the better doping efficiency.

The nature of the doping of DMBI has been studied for C_{60} derivatives by Bao and co-workers[57] and is characterized by a reaction between the dopant and host (fullerene) that begins with either hydride or hydrogen atom transfer and followed by the formation of host radical anions is responsible for the doping effect. Therefore, the energetics of the doping process could be partially determined by the hydride/hydrogen donating ability of the dopant and/or the offset between the DMBI imidazoline SOMO (singly occupied molecular orbital) and the host LUMO. However, the possibility for the increased doping efficiency in doped PTEG-1 system due to the different electron donating ability of two different dopants caused by the side chains could be excluded since: i) According to the study on the organic hydride donors from Cheng and co-workers, [58] dimethylaminio group (-NMe_2) renders a larger enthalpy change of the dopant (N-DMBI) to release a hydride anion than methoxy group (-OMe on MeO-DMBI) does and similar changes for proton-releasing (the probability of which is much smaller than hydride-releasing due to the much higher enthalpy change), this means TEG-DMBI (We assume TEG group effects the electron-donating property of the dopant similarly with methoxy group, the cyclic voltammetry curve of TEG-DMBI shown in supporting information is almost identical to that of MeO-DMBI reported in that paper and higher than that of N-DMBI) should be a weaker hydride donor (than N-DMBI) and consequently leads to lower doping efficiency, which is inconsistent with our findings reported herein; ii) Based on B3LYP/6-31G* calculations performed using GAMESS-UK [59] (calculation details in Supporting Information), the neutral radicals of both dopants (after hydrogen removal)

render similar SOMO levels with -2.54 eV for TEG-DMBI vs -2.34 eV for N-DMBI (which is almost identical to the reported one by Bao and co-workers [37]). N-DMBI radical with higher-lying SOMO level is then supposed to result in a larger offset between the dopant SOMO and the host LUMO and therefore a better doing efficiency would be expected (if the highly energetic radicals are somehow responsible for the doping effect [37]), which is incompatible with our observations as well. We could therefore conclude that the enhanced doping efficiency of TEG-DMBI doped PTEG-1 films is not due to the modification of the electron donating ability caused by different side groups. Furthermore, a benefit from smooth film surface topology (our previous work about N-DMBI doped PCBM and PTEG-1 films already confirms it), [54] which could markedly affect the materials' properties, is also excluded since both N-DMBI and TEG-DMBI doped films show almost identical topology according to AFM measurements (AFM height profiles shown in Supporting Information).

To explore the underlying reason for the enhanced doping efficiency, the morphology of doped films were then investigated by AFM based phase imaging, which provides nanometer-scale information about surface structure, going beyond simple topographical mapping to detect variations in composition, adhesion, friction, viscoelasticity et al. Phase imaging has already been employed for the purpose of elucidating the surface heterogeneity of polymeric materials. [60,61] Fig. 4 shows the phase-contrast AFM images of undoped and doped PTEG-1 films before and after annealing. Different color (phase) represents different composites. Before annealing, the AFM phase image (Fig. 4A) of pure PTEG-1 film exhibited intuitively almost perfect "miscibility", since a single component is present. When mixing with dopants, the surface of the doped PTEG-1 films become heterogeneous with obvious phase islands, but to different extent for N-DMBI and TEG-DMBI respectively. Compared with N-DMBI (Fig. 4B), TEG-DMBI (Fig. 4C) doped film shows

better miscibility between PTEG-1 matrix and dopant, since it is more (phase) homogeneous with smaller RMS phase deviation (1.46 °, *vs* 1.90 ° for N-DMBI, more details in Table S1), which is probably ascribed to the interaction between the TEG chain of the dopant TEG-DMBI and PTEG-1, as it is also found in coarse-grain molecular dynamics simulations (see below). (One could not simply compare the RMS roughness of AFM height profile to determine the heterogeneity, e.g., the RMS height derivation for pure PTEG-1 film is 6.48 nm and for N-DMBI doped film is 6.66 nm with very tiny difference between them, however, the former does show far less heterogeneity than the latter, evidenced from Fig. 4A and 4B). Upon annealing, while obvious heterogeneity occurs for pure PTEG-1 film caused by grain boundaries due to the serious aggregation (see AFM topography images in Supporting Information), the doped films showed improved miscibility, which probably mediated by the resultant fullerene radical anion which shows good miscibility with both dopant and pristine fullerene matrix. N-DMBI and TEG-DMBI doped films thus show almost identical RMS phase derivation (1.38 ° vs 1.45 °) after annealing (Fig. 4E and 4F), though relatively obvious difference (1.90 ° vs 1.46 °) was observed before annealing (Fig. 4B and 4C) . In a word, based on phase imaging AFM, TEG-DMBI doped films before annealing show better miscibility between PTEG-1 matrix and the dopant compared with the films doped with N-DMBI, while the improved miscibility of both films upon annealing is somehow the consequence of the doping. We then temporarily ascribe the different doping efficiency to the different miscibility of the films before annealing when the doping reaction is ready to happen, not after it instead when the doping process is done. In short, the miscibility in the as-prepared state matters to the doping efficiency, not in the annealed state.

In parallel, Martini [62–65] coarse-grain molecular dynamics simulations were performed to investigate the different behavior on miscibility of the two systems. More specifically, solvent evaporation simulations [66,67] were carried out so as to obtain thin film morphologies mimicking the spin coating

procedure. Briefly, the simulations start from a three-component system (PTEG-1:dopant:chloroform, with a 30 mol% dopant fraction) from which the solvent is gradually taken out until a dried film is obtained. Further simulation details are given in the Supporting Information and in Ref. 67. TEG-DMBI shows higher degree of mixing with PTEG-1, as can be seen by visually inspecting typical snapshots of the simulated blends shown in Fig. 5A and 5B. This is quantified by computing the number of contacts between PTEG-1 molecules and the dopant DMBI moieties: a higher number of fullerene-dopant contacts indicates higher likelihood to find a dopant molecule close to a fullerene one, i.e., a more intimately mixed morphology. The results are reported in Fig. 5C, where the number of host-dopant contacts are expressed in percentage (where zero is taken as the number of contacts in a planar heterojunction and 100 is the one computed for a completely intermixed morphology, see also Supporting Information). The number of PTEG-1-DMBI contacts is consistently higher in the case of TEG-DMBI doped PTEG-1 films, which means that more finely intermixed morphologies are obtained in this case. Analyzing the evolution of the morphology during drying, PTEG-1 molecules are found to moderately associate in micelle and bilayer type structures due to the C60-C60 and TEG-TEG interactions (consistent with our previous reported layered structure), [54] while dopant molecules remain very soluble. In the case of TEG-DMBI, however, TEG side chains of the dopant insert in those structures much easier than dimethylamino group for N-DMBI, thus more effectively decreasing the segregation of the dopant and fullerene molecules. This results in better miscibility in the TEG-DMBI doped PTEG-1 system, supporting the argument that better doping efficiency is obtained due to better mixing achieved in the as-cast films.

3. Conclusions

We have developed a promising n-type doping system based on C_{60} derivative with high performance for organic thermoelectric applications. By rational chemical structure modification of dopant/host materials, we have demonstrated a record power factor of 19.1 $\mu Wm^{-1}K^{-}$ for solution processable C_{60} derivatives with one of the highest σ of 1.81 Scm^{-1} to date. Our investigations, including phase imaging AFM measurements and coarse-grain molecular dynamics simulations, reveal that introducing the polar side TEG chain into both the dopant and host materials offers a good miscibility of the blend, which accounts for the high doping efficiency of up to 18% at doing concentration of 20 mol% and thus carrier density and mobility, which are critical to the electrical conductivity. This work provides a new direction to apply the rapidly developed organic semiconductors with high carrier mobilities to the thermoelectric field.

4. Experimental Section

Materials: PETG-1 was synthesized according to our previous work. [66] N-DMBI and PCBM were purchased from Sigma Aldrich and Solenne BV, respectively.

Synthesis of Dopant: The synthesis of the new dopant is straightforward, which was then fully characterized by means of HRMS, NMR and IR (see Supporting Information). To the solution of substituted N,N'-dimethyl-*o*-phenylenediamine (120 mg, 0.88 mmol) [58] in 1 ml of methanol was added 4-(2-(2-(2-ethoxyethoxy)ethoxy)ethoxy)benzaldehyde (280 mg, 0.99 mol) with vigorously shaking at 0 ◦C , then a drop of glacial acetic acid was added. The mixture was allowed to warm to room temperature for 2.5 h, then evaporated to give the crude product which was then purified by column chromatography (Neutral Al2O3, Hexane : DCM= 1:1) to give 200 mg desired product as a white solid (57%).1H-NMR (400 MHz, CD_3OD) δ 7.48 (d, J = 8.6 Hz, 2H),

6.99 (d, J = 8.6 Hz, 2H), 6.65 (dd, J = 5.4, 3.2 Hz, 2H), 6.42 (dd, J = 5.4, 3.2 Hz, 2H), 4.67 (s, 1H), 4.18–4.13 (m, 2H), 3.89–3.82 (m, 2H), 3.71–3.50 (m, 10H), 2.49 (s, 6H), 1.17 (t, J = 7.0 Hz, 3H). ^{13}C-NMR (75 MHz, CD3OD) δ 162.5, 144.8, 133.5, 132.4, 121.8), 116.8, 108.4, 96.6, 73.0, 72.8, 72.1, 72.0, 69.9, 68.8, 34.9, 16.7. IR (cm^{-1}): 2866, 1719, 1606, 1491, 1452, 1367, 1295, 1243, 1112, 728. HRMS(ESI) calcd. for $C_{23}H_{33}N_2O_4[M+H]^+$: 401.24348, found: 401.24184.

Device fabrication: The borosilicate glass substrates were sequentially washed with detergent, acetone and *iso*-propanol, then dried by nitrogen gun and treated with UV-ozone for 20 minutes. The different doped PTEG-1 films were prepared by spin-coating PTEG-1 solution (5 mg/ml in chloroform) after adding different amount of dopant solution (5 mg/ml in chloroform) in glove-box with nitrogen atmosphere. The film thickness (d) falls between 40-50 nm. For the electrical conductivity measurements, parallel line-shape Au electrodes with width (w) of 13 mm and channel length (L) from 100-300 μm were deposited as the top contact. Voltage-sourced two-point conductivity measurements were conducted in the probe station in N_2 glove-box. The electrical conductivity (σ) was calculated according to the formula: $\sigma = (J/V) \times L/(w \times d)$. The conductivity of commercial PEDOT:PSS (Clevios P VP AI 4083) is measured to be 0.06 S/m, which is consistent with the standard value between 0.02 to 0.2 S/m.

Characterization of Thin films: The thicknesses of all the films (≈ 45 nm) were measured by ellipsometry. AFM height and phase images were recorded in tapping using a Bruker MultiMode 8 mi- croscope with TESP probes. The seebeck coefficient was measured by home-built setup (as we reported before [54]) and continuously changed temperature gradient was imposed across the devices to measure the thermal voltage at varying temperature difference.

Coarse-Grain Molecular Dynamics Simulations: Coarse-grain (CG) models are based on the Martini CG force field. [62] On average, four non-hydrogen atoms are mapped to a CG particle (also

termed bead). Eighteen CG particle types (with different levels of polarity) are available to describe the molecules in the coarsegrained space. Interactions between these CG particles have been parametrized based on free energy of transfer data. [62] Atomistic models based on the GROMOS 53A669 force field were used to derive CG bonded parameters. A detailed description of the CG and atomistic models can be found in the Supporting Information. Simulated solution-processed morphologies were obtained by coarse-grain molecular dynamics solvent evaporation simulations. [66,67] Starting from a simulation box (30×30×88 nm^3) containing a ternary mixture PTEG-1:dopant:chloroform (total concentration of 60 mg/ml; 30% molar dopant fraction), 1.25% of the amount of chloroform is removed every 30 ns until a dried morphology is obtained (30×30×~5 nm^3). 3D periodic boundary conditions are applied. The total drying time amounts to 19 ms. A time step of 20 fs was used to integrate the equations of motion, while the box dimensions were fixed in the lateral directions by setting the compressibility to 0 bar^{-1}. All the other simulation parameters are listed exhaustively in Ref. 67, and correspond to the “new" Martini set of run parameters.70 All simulations were run using the GROMACS 5.x package.[71] All files needed to run the solvent evaporation simulations are available for download as part of the Supporting Information and on the Martini portal http://cgmartini.nl.

Acknowledgement

This work is part of the research programme of the Foundation of Fundamental Research on Matter (FOM), which is part of the Netherlands Organisation for Scientific Research (NWO). This is a publication by the FOM Focus Group ‘Next Generation Organic Photovoltaics’, participating in the Dutch Institute for Fundamental Energy Research (DIFFER). R.A. thanks NWO (Graduate Programme Advanced Materials, No. 022.005.006) for financial support and Alex H. de Vries and

Paulo C. T. Souza for insightful discussions. Computational resources for this work were partly provided by the Dutch National Supercomputing Facilities through NWO.

References

1 L. E. Bell, Science, 2008, 321, 1457–1461.

2 J. R. Sootsman, D. Y. Chung and M. G. Kanatzidis, Angewandte Chemie International Edition, 2009, 48, 8616–8639.

3 A. Shakouri, Annual Review of Materials Research, 2011, 41, 399–431.

4 M. Zebarjadi, K. Esfarjani, M. Dresselhaus, Z. Ren and G. Chen, Energy & Environmental Science, 2012, 5, 5147– 5162.

5 J. Yang, H.-L. Yip and A. K.-Y. Jen, Advanced Energy Materials, 2013, 3, 549–565.

6 R. Ovik, B. Long, M. Barma, M. Riaz, M. Sabri, S. Said, R. Saidur et al., Renewable and Sustainable Energy Reviews, 2016, 64, 635–659.

7 C. O'Dwyer, R. Chen, J.-H. He, J. Lee and K. M. Razeeb, ECS Journal of Solid State Science and Technology, 2017, 6, N3058–N3064.

8 B. Russ, A. Glaudell, J. J. Urban, M. L. Chabinyc and R. A. Segalman, Nature Reviews Materials, 2016, 1, 16050.

9 D. Beretta, A. Perego, G. Lanzani and M. Caironi, Sustainable Energy & Fuels, 2017.1,174-190.

10 Y. Sun, W. Xu, C.-a. Di and D. Zhu, Synthetic Metals, 2017, 225, 22–30.11 N. Kim, B. Domercq, S. Yoo, A. Christensen, B. Kippelen and S. Graham, Applied Physics Letters, 2005, 87, 241908.

11 N. Kim, B. Domercq, S. Yoo, A. Christensen, B. Kippelen and S. Graham, Applied Physics Letters , 2005, 87, 241908.

12 Y. Jin, A. Yadav, K. Sun, H. Sun, K. Pipe and M. Shtein, Applied physics letters, 2011, 98, 48.

13 Y. Jin, C. Shao, J. Kieffer, K. P. Pipe and M. Shtein, Journal of Applied Physics, 2012, 112, 093503.

14 J. C. Duda, P. E. Hopkins, Y. Shen and M. C. Gupta, Applied Physics Letters, 2013, 102, 251912.

15 Y. Jin, S. Nola, K. P. Pipe and M. Shtein, Journal of Applied Physics, 2013, 114, 194303.

16 X. Wang, C. D. Liman, N. D. Treat, M. L. Chabinyc and D. G. Cahill, Physical Review B, 2013, 88, 075310.

17 S. Bhattacharya, A. Pope, R. Littleton IV, T. M. Tritt, V. Ponnambalam, Y. Xia and S. Poon, Applied Physics Letters, 2000, 77, 2476–2478.

18 D. Vashaee and A. Shakouri, physical review letters, 2004, 92, 106103.

19 J.-H. Lee, J. Wu and J. C. Grossman, Physical review letters, 2010, 104, 016602.

20 M. Zebarjadi, G. Joshi, G. Zhu, B. Yu, A. Minnich, Y. Lan, X. Wang, M. Dresselhaus, Z. Ren and G. Chen, Nano letters, 2011, 11, 2225–2230.

21 B. Yu, M. Zebarjadi, H. Wang, K. Lukas, H. Wang, D. Wang, C. Opeil, M. Dresselhaus, G. Chen and Z. Ren, Nano letters, 2012, 12, 2077–2230.

22 D. Maddison, J. Unsworth and R. Roberts, Synthetic metals, 1988, 26, 99–108.

23 Y. Hiroshige, M. Ookawa and N. Toshima, Synthetic Metals, 2007, 157, 467–474.

24 K. Pernstich, B. Rössner and B. Batlogg, Nature materials, 2008, 7, 321–325.

25 O. Bubnova, Z. U. Khan, A. Malti, S. Braun, M. Fahlman, M. Berggren and X. Crispin, Nature materials, 2011, 10, 429– 433.

26 G. Kim, L. Shao, K. Zhang and K. P. Pipe, Nature Materials, 2013, 12, 719–723.

27 R. A. Schlitz, F. G. Brunetti, A. M. Glaudell, P. L. Miller, M. A. Brady, C. J. Takacs, C. J. Hawker and M. L. Chabinyc, Ad- vanced Materials, 2014, 26, 2825–2830.

28 J. Loureiro, N. Neves, R. Barros, T. Mateus, R. Santos, S. Filonovich, S. Reparaz, C. M. Sotomayor-Torres, F. Wyczisk, L. Divay et al., Journal of Materials Chemistry A, 2014, 2, 6649–6655.

29 S. N. Patel, A. M. Glaudell, D. Kiefer and M. L. Chabinyc, ACS Macro Letters, 2016, 5, 268–272.

30 O. Bubnova, M. Berggren and X. Crispin, Journal of the American Chemical Society, 2012, 134, 16456–16459.

31 Q. Zhang, Y. Sun, W. Xu and D. Zhu, Energy & Environmental Science, 2012, 5, 9639–9644.

32 K. Park, K. Ahn, J. Cha, S. Lee, S. I. Chae, S.-P. Cho, S. Ryee, J. Im, J. Lee, S.-D. Park et al., Journal of the American Chemical Society, 2016.138, 14458–14468

33 Y. Sun, P. Sheng, C. Di, F. Jiao, W. Xu, D. Qiu and D. Zhu, Advanced Materials, 2012, 24, 932–937.

34 B. Russ, M. J. Robb, F. G. Brunetti, P. L. Miller, E. E. Perry, S. N. Patel, V. Ho, W. B. Chang, J. J. Urban, M. L. Chabinyc et al., Advanced Materials, 2014, 26, 3473–3477.

35 S. Wang, H. Sun, U. Ail, M. Vagin, P. O. Ã. Persson, J. W. Andreasen, W. Thiel, M. Berggren, X. Crispin, D. Fazzi and S. Fabiano, Advanced Materials, 2016, 10764–10771.

36 K. Pudzs, A. Vembris, M. Rutkis and S. Woodward, Advanced Electronic Materials, 2017, 3, 1600429.

37 P. Wei, J. H. Oh, G. Dong and Z. Bao, Journal of the American Chemical Society, 2010, 132, 8852–8853.

38 P. Wei, N. Liu, H. R. Lee, E. Adijanto, L. Ci, B. D. Naab, J. Q. Zhong, J. Park, W. Chen, Y. Cui et al., Nano letters, 2013, 13, 1890anced

39 H. Wang, P. Wei, Y. Li, J. Han, H. R. Lee, B. D. Naab, N. Liu, C. Wang, E. Adijanto, B. C.-K. Tee et al., Proceedings of the National Academy of Sciences, 2014, 111, 4776–4781.

40 B. D. Naab, S. Zhang, K. Vandewal, A. Salleo, S. Barlow, S. R. Marder and Z. Bao, Advanced Materials, 2014, 26, 4268–4272.

41 B. D. Naab, X. Gu, T. Kurosawa, J. W. To, A. Salleo and Z. Bao, Advanced Electronic Materials, 2016, 2, 1600004.

42 K. Shi, F. Zhang, C.-A. Di, T.-W. Yan, Y. Zou, X. Zhou, D. Zhu, J.-Y. Wang and J. Pei, Journal of the American Chemical Society, 2015, 137, 6979–6982.

43 J. E. Anthony, A. Facchetti, M. Heeney, S. R. Marder and X. Zhan, Advanced Materials, 2010, 22, 3876–3892.

44 G. Yu, J. Gao, J. Hummelen, F. Wudl and A. Heeger, Science, 1995, 270, 15.

45 C. J. Brabec, N. S. Sariciftci, J. C. Hummelen, Advanced functional materials, 2001, 11, 15-26.

46 J. Zaumseil and H. Sirringhaus, Chemical reviews, 2007, 107, 1296–1323.

47 D. M. Guldi, B. M. Illescas, C. M. Atienza, M. Wielopolski and N. Martín, Chemical Society Reviews, 2009, 38, 1587–1597.

48 A. Hebard, M. Rosseinky, R. Haddon, D. Murphy, S. Glarum, T. Palstra, A. Ramirez and A. Karton, Nature, 1991, 350, 600– 601.

49 T. Inabe, H. Ogata, Y. Maruyama, Y. Achiba, S. Suzuki, K. Kikuchi and I. Ikemoto, Physical review letters, 1992, 69, 3797.

50 Z. Wang, K. Ichimura, M. Dresselhaus, G. Dresselhaus, W.-T. Lee, K. Wang and P. Eklund, Physical Review B, 1993, 48, 10657.

51 M. Sumino, K. Harada, M. Ikeda, S. Tanaka, K. Miyazaki and C. Adachi, Applied Physics Letters, 2011, 99, 093308.

52 T. Menke, D. Ray, J. Meiss, K. Leo and M. Riede, Applied Physics Letters, 2012, 100, 093304.

53 A. Barbot, C. Di Bin, B. Lucas, B. Ratier and M. Aldissi, Journal of Materials Science, 2013, 48, 2785–2789.

54 J. Liu, L. Qiu, G. Portale, G. T. Brink, J. C. Hummelen, and L. J. A. Koster, 2017, DOI: 10.1002/adma.201701641.

55 W. Pasveer, J. Cottaar, C. Tanase, R. Coehoorn, P. Bobbert, P. Blom, D. De Leeuw and M. Michels, Physical review letters, 2005, 94, 206601.

56 G. Garcia-Belmonte, P. P. Boix, J. Bisquert, M. Sessolo and H. J. Bolink, Solar Energy Materials and Solar Cells, 2010, 94, 366–375.

57 B. D. Naab, S. Guo, S. Olthof, E. G. Evans, P. Wei, G. L. Mill- hauser, A. Kahn, S. Barlow, S. R. Marder and Z. Bao, Journal of the American Chemical Society, 2013, 135, 15018–15025.

58 X.-Q. Zhu, M.-T. Zhang, A. Yu, C.-H. Wang and J.-P. Cheng, Journal of the American Chemical Society, 2008, 130, 2501–2516.

59 M. F. Guest, I. J. Bush, H. J. J. van Dam, P. Sherwood, J. M. H. Thomas, J. H. van Lenthe, R. W. A. Havenith and J. Kendrick, Mol. Phys., 2005, 103, 719–747.

60 D. Raghavan, X. Gu, T. Nguyen, M. VanLandingham and A. Karim, Macromolecules, 2000, 33, 2573–2583.

61 D. Raghavan, M. VanLandingham, X. Gu and T. Nguyen, Langmuir, 2000, 16, 9448–9459.

62 S. J. Marrink, H. J. Risselada, S. Yefimov, D. P. Tieleman and A. H. de Vries, The Journal of Physical Chemistry B, 2007, 111, 7812–7824.

63 L. Monticelli, Journal of Chemical Theory and Computation, 2012, 8, 1370–1378.

64 G. Rossi, P. F. J. Fuchs, J. Barnoud and L. Monticelli, The Journal of Physical Chemistry B, 2012, 116, 14353–14362.

65 T. Winands, M. Bockmann, T. Schemme, P.-M. T. Ly, D. H. de Jong, Z. Wang, C. Denz, A. Heuer and N. L. Doltsinis, Physical Chemistry Chemical Physics, 2016, 18, 6217–6227.

66 C.-K. Lee and C.-W. Pao, The Journal of Physical Chemistry C, 2014, 118, 11224–11233.

67 R. Alessandri, J. J. Uusitalo, A. H. de Vries, R. W. A. Havenith and S. J. Marrink, Journal of the American Chemical Society, 2017, 139, 3697–3705.

68 F. Jahani, S. Torabi, R. C. Chiechi, L. J. A. Koster and J. C. Hummelen, Chemical Communications, 2014, 50, 10645–10647.

69 C. Oostenbrink, A. Villa, A. E. Mark and W. F. van Gunsteren, Journal of Computational Chemistry, 2004, 25, 1656–1676.

70 D. H. de Jong, S. Baoukina, H. I. Ingólfsson and S. J. Marrink, Computer Physics Communications, 2016, 199, 1–7.

71 M. J. Abraham, T. Murtola, R. Schulz, S. Páll, J. C. Smith, B. Hess and E. Lindahl, SoftwareX, 2015, 1, 19–25.

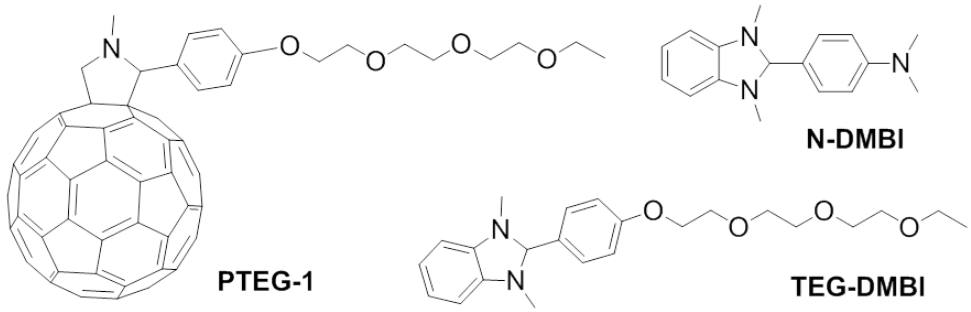

Fig. 1 Chemical structures of PTEG-1, N-DMBI and TEG-DMBI.

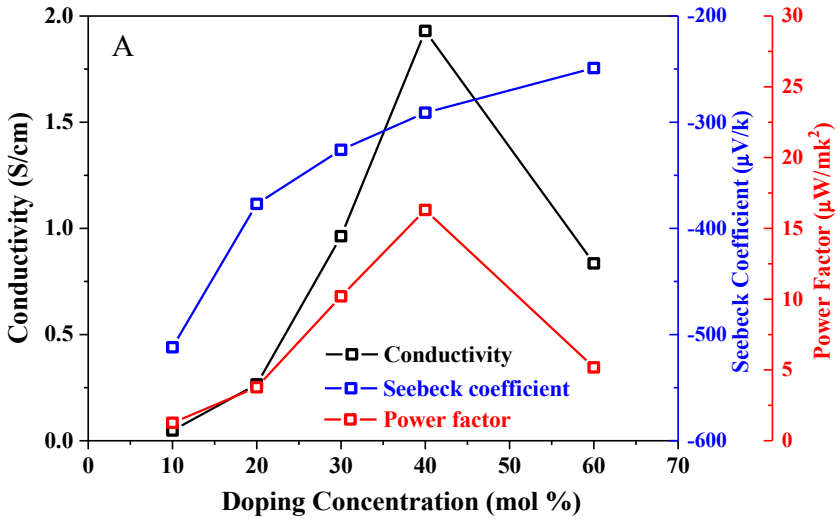

Fig. 2 The measured Seebeck coefficient (blue), electrical conductivity (black) and power factor (red) as a function of doping concentration in N-DMBI (A) and TEG-DMBI (B) doped PTEG-1 films.

Table 1 The thermoelectric parameters of the different doped PTEG-1 films at room temperature.

Sample	Dopant weight (mol %)	σ [S/cm]	S [$\mu V/k$]	σS^2 [$\mu W/mk^2$]
TEG-DMBI	5	0.0008	-	-
	10	0.07	-512	1.84
	20	1.81	-325	19.1
	30	1.42	-302	12.9
	40	1.01	-294	8.69
	60	0.67	-286	5.47
N-DMBI	10	0.05	-512	1.26
	20	0.27	-377	3.77
	30	0.96	-326	10.2

	40	1.93	-291	16.3
	60	0.84	-249	5.18

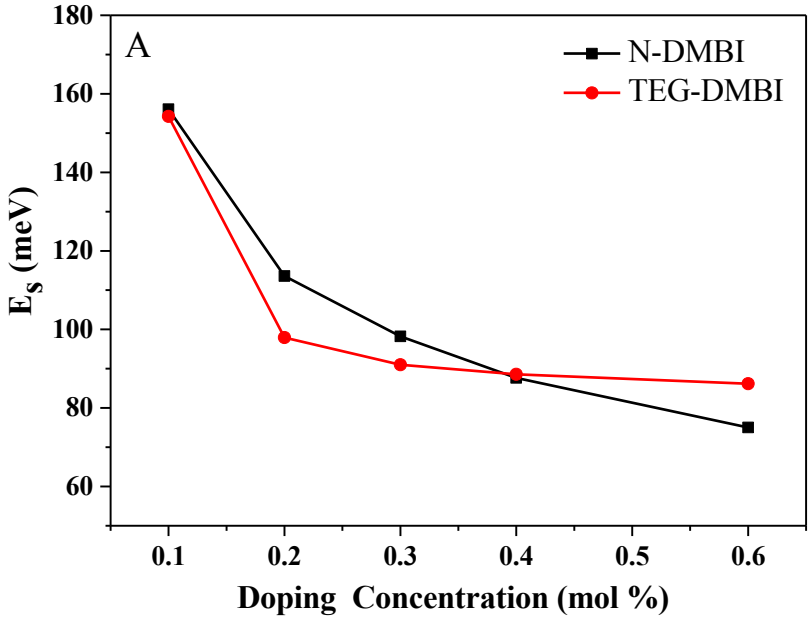

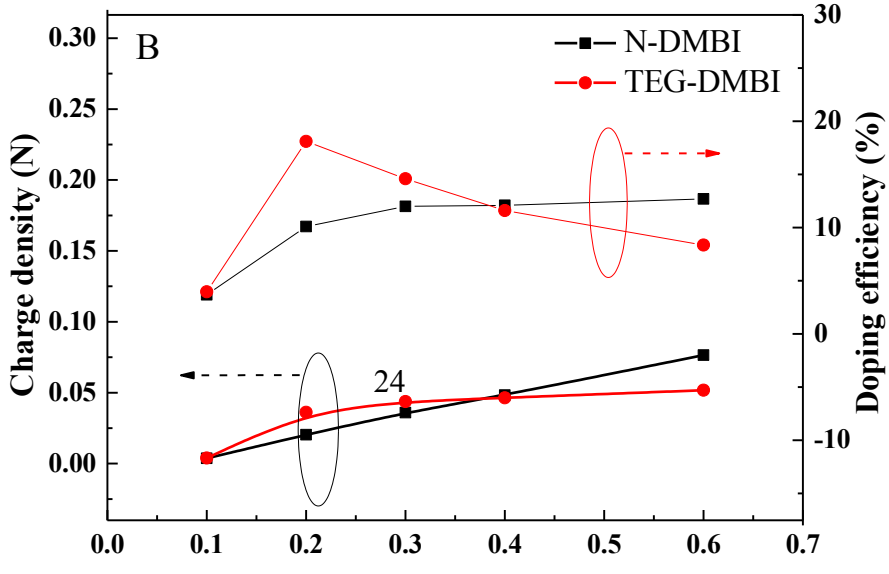

Fig. 3 Es evolution (A) and Charge carrier densities and doping efficiency (defined as the percentage of free carriers formed per added dopant molecule) evolution (B) with different doping concentration in different N-DMBI and TEG-DMBI doped PTEG-1 films.

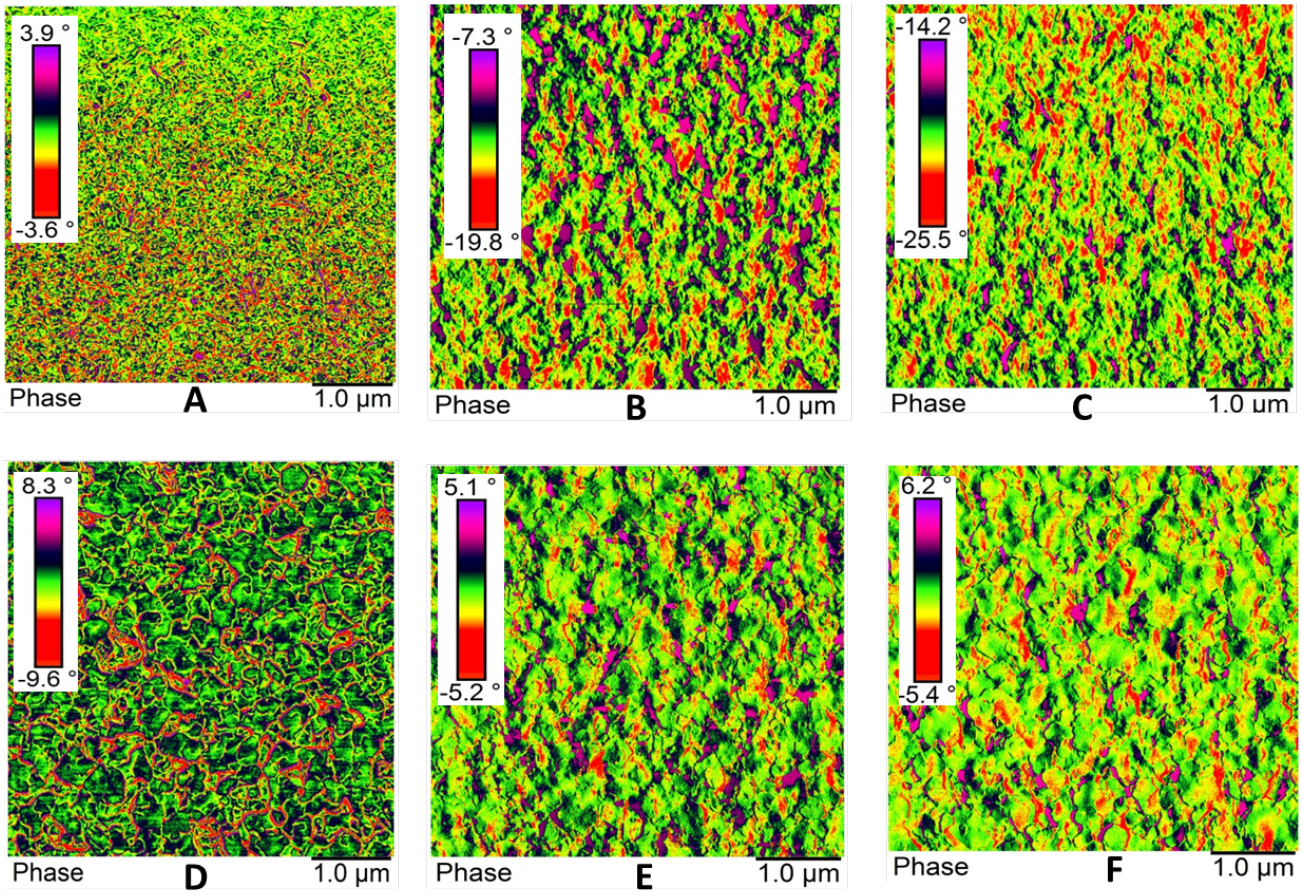

Fig. 4 AFM phase images of PTEG-1 films before (up) and after (below) annealing at 120 °C for 1.5 h without (**A,D**) and with 30 molar% dopants (N-DMBI (**B,E**), TEG-DMBI (**C,F**)).

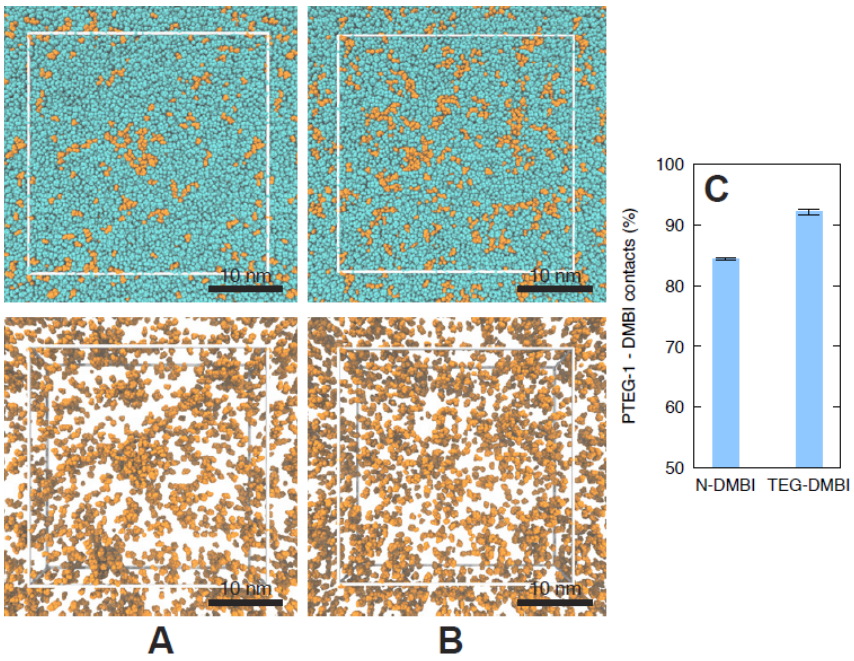

Fig. 5 Simulated morphology for N-DMBI (**A**) and TEG-DMBI (**B**) doped PTEG-1 films. PTEG-1 molecules are shown in cyan, while dopant molecules in orange (top). Only DMBI backbones are shown in the bottom renderings. Number of contacts between PTEG-1 molecules and DMBI backbones, which correlate with the degree of fullerene-dopant mixing in the morphologies, are also shown (**C**).